OPEN

Reactive co-sputter deposition of Ta-doped tungsten oxide thin films for water splitting application

Samaneh Jafarpour & Hamid Naghshara✉

This study aimed to investigate the structural, optical, and electronic properties of WO_3 thin films modified by Ta-doping, considering their potential application in photoelectrochemical (PEC) water splitting. Due to its unique physical and chemical properties, WO_3 films have been commonly suggested as a promising photoanode for hydrogen production. However, the wide bandgap and unsuitable band edge positions of WO_3 limit its PEC efficiency. Doping have been extensively applied as an effective strategy for bandgap engineering. Here, post-annealed WO_3 films with different concentrations of Ta dopant were synthesized via reactive magnetron co-sputtering, while DC and RF sputtering powers were varied with the aim of achieving the desired properties. EDX analysis showed that Ta atoms were doped into WO_3 in the range of 0–3.93 at%. As evident from SEM and AFM images, the surface morphology was significantly affected by increasing Ta doping, the formation of a granular structure with well-defined boundaries and increasing surface roughness (1.79–47.94 nm). XRD patterns confirmed that the incorporation of Ta atoms into a monoclinic WO_3 improved the crystallinity, especially in the (002) direction. Most importantly, a decrease in the average transparency (92.82–74.27%), an increase in visible absorption, a red shift of the fundamental absorption edge corresponding to a favorable drop in the optical bandgap energy (3.07–2.61 eV) were found with increasing Ta concentration. Notably, the substitution of W^{6+} ions with Ta dopant (0–3.93 at%) led to an upward shift in the valence band maximum (3.62–3.31 eV) and a downward shift in the conduction band minimum (0.55–0.70 eV). The WO_3 photoanode doped with 3.93 at% Ta exhibited the maximum photocurrent density of 0.65 mA/cm^2 (at 1 V vs. Ag/AgCl) under simulated sunlight. Furthermore, WO_3 photoanode doped with 3.93 at% Ta showed excellent photoresponsivity and slow electron–hole recombination. The obtained results predict the potential of Ta-doping coupled with post-annealing to optimize the structural and optoelectronic properties of sputtered WO_3 thin films as photoanode for use in efficient PEC water splitting.

Keywords WO_3, Ta-doping, Photoelectrochemical water splitting, Bandgap, Co-sputtering, Photocurrent

Nowadays, rising global energy consumption and the depletion of fossil fuels have become great challenges for humanity[1]. In addition, the combustion of fossil fuels leads to important environmental damages such as water and air pollution, global warming due to increased CO_2 concentration in the atmosphere, and the greenhouse effect[2,3]. Therefore, it is necessary to find renewable, sustainable, and clean energy systems to meet future energy needs along with environmental protection[4,5]. Recently, hydrogen (H_2) has attracted considerable attention as a ultimate clean and renewable energy source with the potential to be used in fuel cells and chemical industries without emitting toxic gases (CO_x, NO_x, SO_x, C_xH_y)[5–7]. Extraction of hydrogen from water and sunlight through photoelectrochemical (PEC) water splitting has been recognized as an efficient solution for solar energy utilization[8,9]. The interesting discovery of the PEC water splitting was first reported in 1972 by Fujishima and Honda using a titanium dioxide photoanode[10]. Recently, the identification, development, and exploitation of ideal photoanode materials with a suitable designs to achieve better water splitting activity have been investigated[11–15]. To realize the most efficient PEC water splitting, semiconductors must possess essential properties, including adequate visible light absorption, effective charge separation and transportation, enhanced photocarrier collection, efficient water reduction and oxidation catalysis, and well stability in acid[16]. Numerous amount of research has been devoted to the use of metal oxide semiconductors such as TiO_2[17], ZnO[18], NiO[19], α-Fe_2O_3[20], Cu_2O[21], Cu/CuO[22], CuO-La_2O_3[23], CeO_2[24], SnO_2[25], $BiVO_4$[26], $NaTaO_3$[27], $KTaO_3$[28], $SrTiO_3$[29], and $CuFeO_2$[30], $LaFeO_3$[31], and $CuBi_2O_4$[32] in PEC water splitting. Among these metal oxides, n-type semiconductor tungsten oxide (WO_3) has attracted considerable attention due to its potential applications in optoelectronic

Faculty of Physics, University of Tabriz, Tabriz, Iran. ✉email: naghshara@tabrizu.ac.ir

devices, gas sensors, optical detectors, electrochromic devices, solar cells, supercapacitors, high-temperature diodes, photocatalysts, MIS-based devices, hydrophilic coatings, schottky barrier diodes, etc.[33–37] Furthermore, tungsten oxide is well-known as the promising electrode material for efficient solar-to-H_2 conversion because of several advantages including, availability, non-toxicity, photosensivity, tunable bandgap, fast carrier transport, medium hole diffusion length, excellent photocorrosion resistance in aqueous solutions, high chemical stability, and inexpensive[38–41]. The first successful realization of solar water splitting on tungsten oxide photoanode was reported by Hodes el al.[42]. After that, many researchers have focused on the synthesis of tungsten oxide with favorable optical, electrical, and mechanical properties. Tungsten oxide is more preferred than ZnO and TiO_2 for PEC water splitting[43]. According to reports, WO_3 can absorb almost 12% of the solar spectrum, which provides the maximum efficiency (~ 4.8%) of solar-to-hydrogen conversion in PEC systems[44]. Despite these features, the implementation of highly efficient water splitting reaction by tungsten oxide faces major limitations. First, the bandgap of tungsten oxide is not narrow enough to absorb a significant part of sunlight[45]. On the other hand, the position of the conduction band edge is not higher according to the redox potential of H^+/H_2, so the excited electrons in the conduction band are not able to convert protons into hydrogen[46]. Consequently, band edge engineering is required to narrow the bandgap and alter the band levels of WO_3[47]. Numerous methods have been proposed for band edge engineering, such as metal doping, morphological control, composite material production, and surface sensitization[48]. Among these, doping with metal ions is suggested as the most effective approach to tune the optical and electrical properties of metal oxides[48]. Recently, doping of WO_3 with metal ions such as Mg[49], Ti [50,51], Zr[52], Ta[53], Mo[54], Fe[55], Ni[56], Cu[57], Al[58], Ga[59], Sn[60], Bi[61], Te[62], and Gd[63] has been extensively investigated. Since the radius of Ta ions is close to that of tungsten, they are properly incorporated into the tungsten lattice. As a result, it assumed that the doping of Ta metal ions into tungsten oxide can easily reduce the optical band gap and improve the photoconversion efficiency[64]. There are various techniques to produce metal-ion-doped WO_3 thin films including, hydrothermal[65], sol–gel[66], electrodeposition[67], spray pyrolysis[68], electron beam evaporation[69], thermal evaporation[70], and magnetron sputtering[71]. In the present work, the reactive magnetron co-sputtering method is applied for the deposition of Ta-doped tungsten oxide thin films with various Ta content. This method provides film deposition with uniform thickness, high purity, homogeneous surface, better adhesion to the substrate, large-area scale, and desired dopant concentration at room temperature[72–75]. Different DC and RF sputtering powers have been applied to W and Ta metal targets, respectively. The variation of the sputtering powers enables us to adjust the composition (Ta/W ratio) of the samples to achieve suitable optoelectronic properties for applications in water splitting. Here, the annealing process is necessary to form crystalline WO_3 for better PEC activity. Based on earlier studies, annealing conditions and temperature were selected[76]. The effect of Ta-doping and post-annealing on the structural, morphological, optical, and electronic characteristics of sputtered WO_3 thin films was analyzed in detail.

Methodology

Thin films of Ta_2O_5, WO_3, and Ta-doped WO_3 were synthesized through reactive magnetron co-sputtering technique under Ar/O_2 atmosphere at room temperature using a MECA-2000 system, as shown in Fig. 1. Tungsten (W) and Tantalum (Ta) metal targets (99.99% purity, 6 mm thickness, and 76.2 mm diameter) were attached to DC and RF supplied magnetrons, respectively. Glass and quartz substrates (1×1 cm^2) were successively cleaned in an ultrasonic bath according to the standard protocol by acetone, ethanol, and deionized water for 15 min and then dried with N_2 gas. To ensure the uniformity of film deposition, the substrates were placed in a holder rotating at 30 rpm. The substrates were fixed at a distance of 15 cm from the target. The synthesis chamber was evacuated using rotary and turbomolecular pumps to reach a pressure of 4.9×10^{-5} mbar. The targets were pre-sputtered to remove surface contaminations in a pure argon plasma for 10 min. The flow of Ar gas was kept at 25 sccm, simultaneously, O_2 was introduced the chamber as reactive gas with the flow of 6.25 sccm. The flow of gases was controlled by mass flow controllers (MKS-Instruments) with an accuracy of 0.01 sccm. The working pressure during the deposition was carefully tuned at 7×10^{-3} mbar by a stepper motor-controlled high-vac gate valve (VAT PM-5). The DC and RF sputtering powers were varied to control the concentration of W and Ta (at%) in the film composition. Sputtering conditions were mentioned in Table 1. Variable RF power (10–60 W) was applied to the tantalum target in order to incorporate different concentrations of Ta atoms into the tungsten oxide structure to achieve the desired properties. The thickness of the films was determined by vibrating quartz method (MAXTEK, TM-350) about 200 nm. Afterward, the as-deposited samples were annealed at 550 °C for 120 min in a furnace with a heating/cooling ramp (rest) of 8 °C/min in the air ambient. Energy dispersive X-ray spectroscopy (EDX, Tescan-Mira III) was employed to detect the elemental composition of the prepared thin films. The surface morphology of the samples was observed by a field emission scanning electron microscope (FESEM, Tescan-Mira III). The surface topography and roughness of the films were investigated using an atomic force microscope (AFM, Nanosurf mobile S). X-ray diffraction (XRD, Siemens D500) was employed to investigate the crystalline structure of the prepared samples. UV–Vis spectra were collected by spectrophotometer (GENESYS-5) in the wavelength range of 200–1100 nm. From the recorded data, optical parameters such as fundamental absorption edge and band gap energy were obtained. The photoelectrochemical performance of the prepared samples were measured using a conventional three-electrode setup under 1.5 G illumination of a 100 W Xe lamp. For PEC studies, undoped and Ta-doped WO_3 thin films were depositied on indium tin oxide (ITO) (200 nm) coated quartz substrates, which acted as working electrode. The area exposed to light was set to 1 cm^2 for all samples. A platinum wire was applied as a counter electrode, and a saturated Ag/AgCl was used as a reference electrode. Photocurrent measurements were conducted using a linear sweep voltammograms (LSV) in the potential range of -0.3 to 1.8 V (vs. Ag/AgCl) with a scan rate of 20 mV/s at room temperature in a 0.2 M Na_2SO_4 electrolyte. The dependency of photocurrent on irradiation-time were evaluate using a two-electrode setup under on/off light illumination at 0 V bias. The measurements were conducted directly between the the pt wire and the samples.
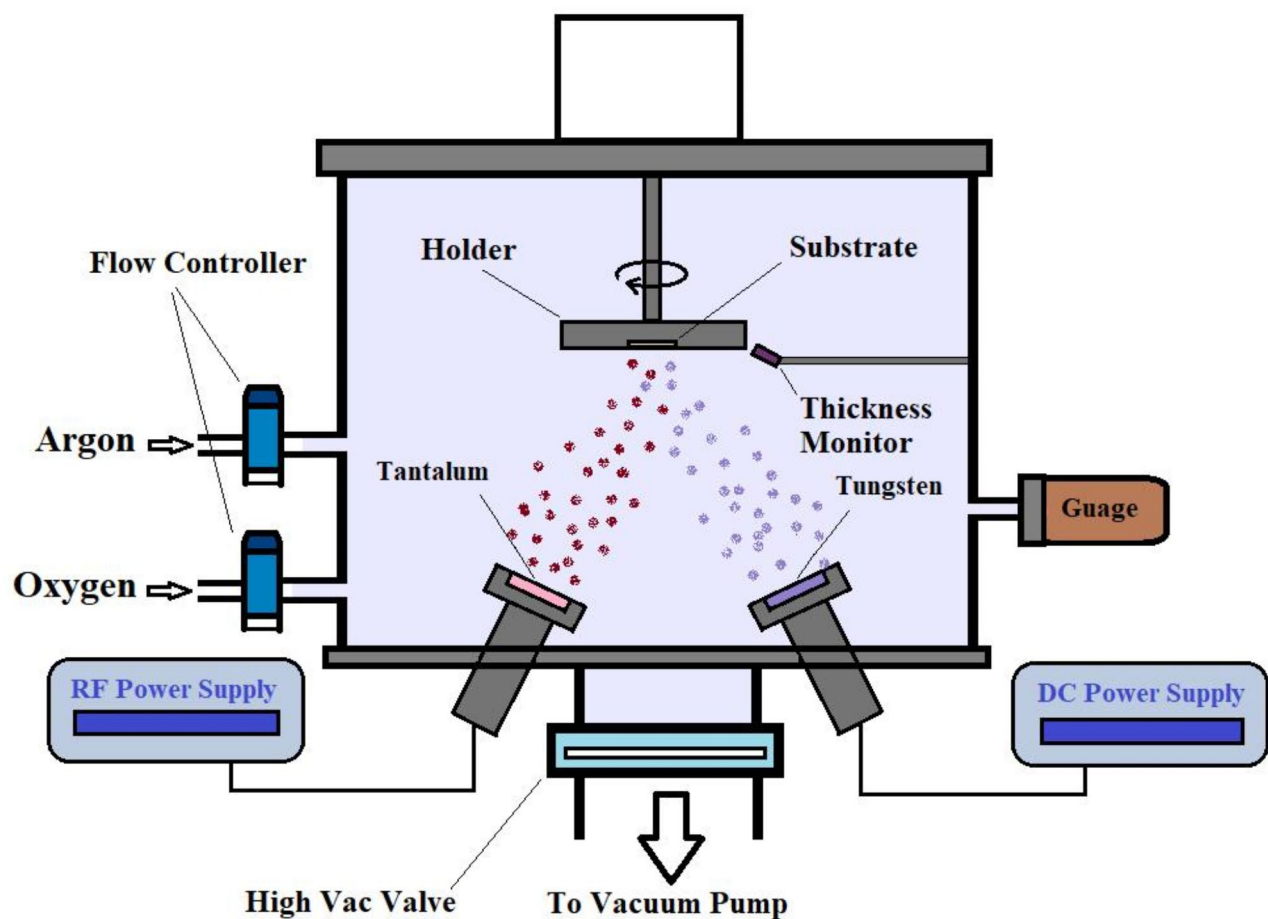
**Fig. 1**. Schematic illustration of the reactive magnetron co-sputtering system.

Thin film	DC power (W)	RF power (W)	Deposition rate (A/S)
Ta_2O_5	0	100	0.1
WO_3	100	0	1.1
Ta-WO_3 (I)	90	10	1
Ta-WO_3 (II)	70	30	0.9
Ta-WO_3 (III)	60	40	0.7
Ta-WO_3 (IV)	40	60	0.3

Table 1. Sputtering deposition conditions.

Results and discussion

Morphological analysis

The compositional analysis of the prepared samples was performed using EDX spectroscopy. Figure 2 depicts the detailed EDX spectrum for the Ta-doped WO_3(IV) sample, indicating the existence of W, Ta, and O elements as reported[77]. The elemental quantification of Ta_2O_5, WO_3, and Ta-doped WO_3 thin films annealed at 550 °C is presented in the inset table of Fig. 2. According to the obtained data, the incorporation of Ta in the doped WO_3 films is evident. The concentration of Ta in doped WO_3 films increases from 0.63 to 3.93% as atomic percentage with increasing RF sputtering power (10 to 60 W). Figure 3 shows surface FESEM micrographs of Ta_2O_5, WO_3, and Ta-doped WO_3 thin films annealed at 550 °C. The surface of undoped Ta_2O_5 and WO_3 films appeared to be smooth, dense, crack-free, and uniform, as shown in Fig. 3a,b. Morphological changes with cracking were significant for Ta-doped WO_3 films after annealing at 550 °C, Fig. c–f. This can be attributed to the improved crystallinity after Ta doping, as observed by XRD patterns. It was found that cracks in the surface morphology of Ta-doped thin films became more prominent with increasing Ta concentration. With further increase in Ta concentration to 3.93 at%, a granular structure with well-defined boundaries and close-packed grains was observed. It is concluded that the surface morphology of Ta-doped WO_3 thin films was significantly affected by the annealing process compared to pure Ta_2O_5 and WO_3. Further morphological characterization
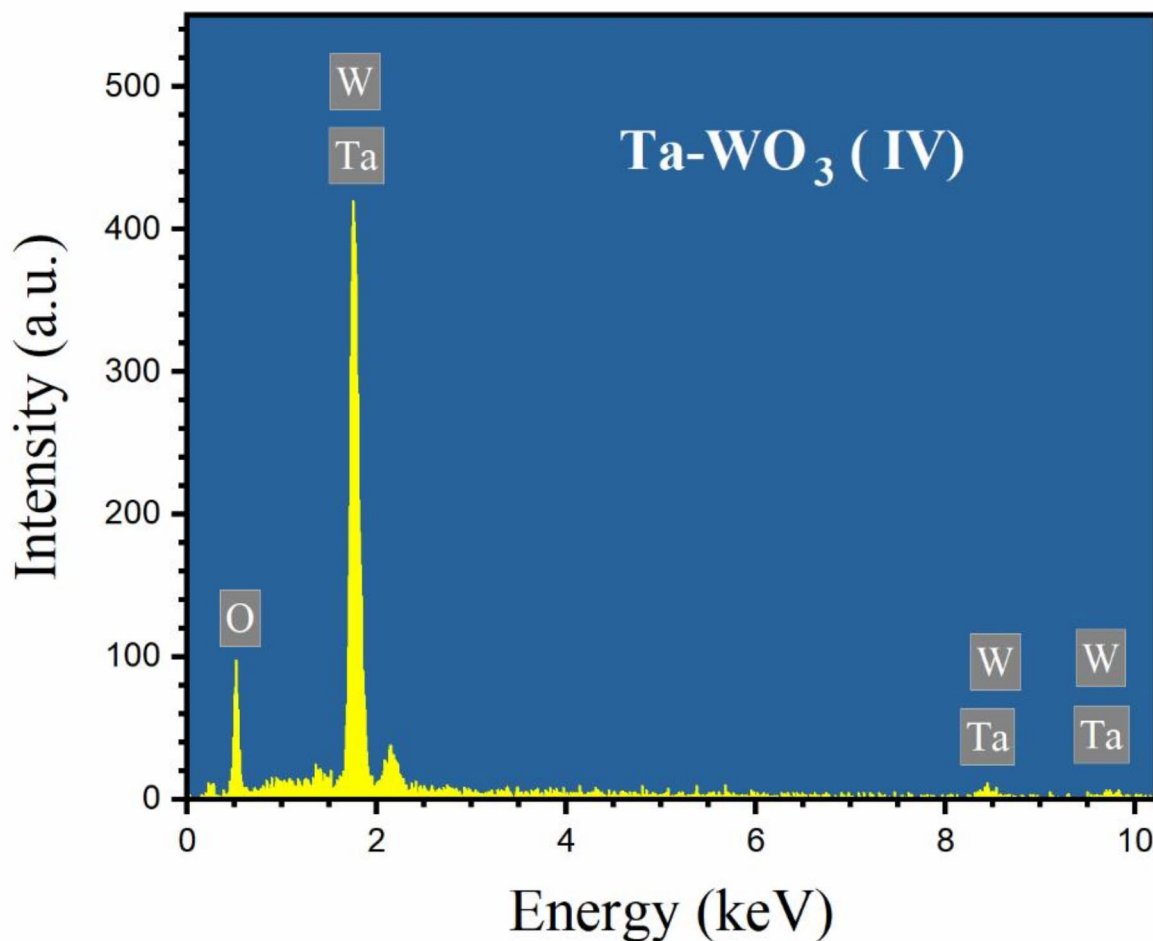
Sample	W (At%)	Ta (At%)
Ta₂O₅	0	29.78
WO₃	13.56	0
Ta-WO₃ (I)	14.33	0.63
Ta-WO₃ (II)	10.73	2.06
Ta-WO₃ (III)	9.35	3.27
Ta-WO₃ (IV)	8.46	3.93

Fig. 2. EDX spectrum of Ta-doped WO_3 (IV) thin film annealed at 550 °C (top) and atomic percentage of identified elements from the EDX spectra (down).

of the prepared samples was performed by AFM analysis. Figure 4 shows two-dimensional (2D) and three-dimensional (3D) AFM images of Ta_2O_5, WO_3, and Ta-doped WO_3 thin films annealed at 550 °C. The surface roughness of the prepared samples was measured in the term of root-mean-square (σ_{rms}) roughness, as presented in Table 2. It was found that undoped Ta_2O_5 and WO_3 thin films have uniform and smooth surfaces with root-mean-squared roughness (σ_{rms}) values of 1.79 nm and 1.98 nm, respectively. Cracked surface morphology with high roughness ($\sigma_{rms} \sim 14.71$–47.94 nm) was found was observed for Ta-doped WO_3 thin films, as confirmed by SEM images. Figure 5 displays the increasing trend of the σ_{rms} value with increasing Ta concentration. This result suggests that Ta doping combined with annealing can form rough surfaces that are preferred for water splitting application[78]. Memar et al. reported that increasing the surface roughness can contribute to increasing the electrolyte/electrode contact area, which leads to the enhancement of photocurrent density. On the other hand, a rough surface allows a large portion of sunlight to be captured due to multiple scattering[79]. Similarly, new
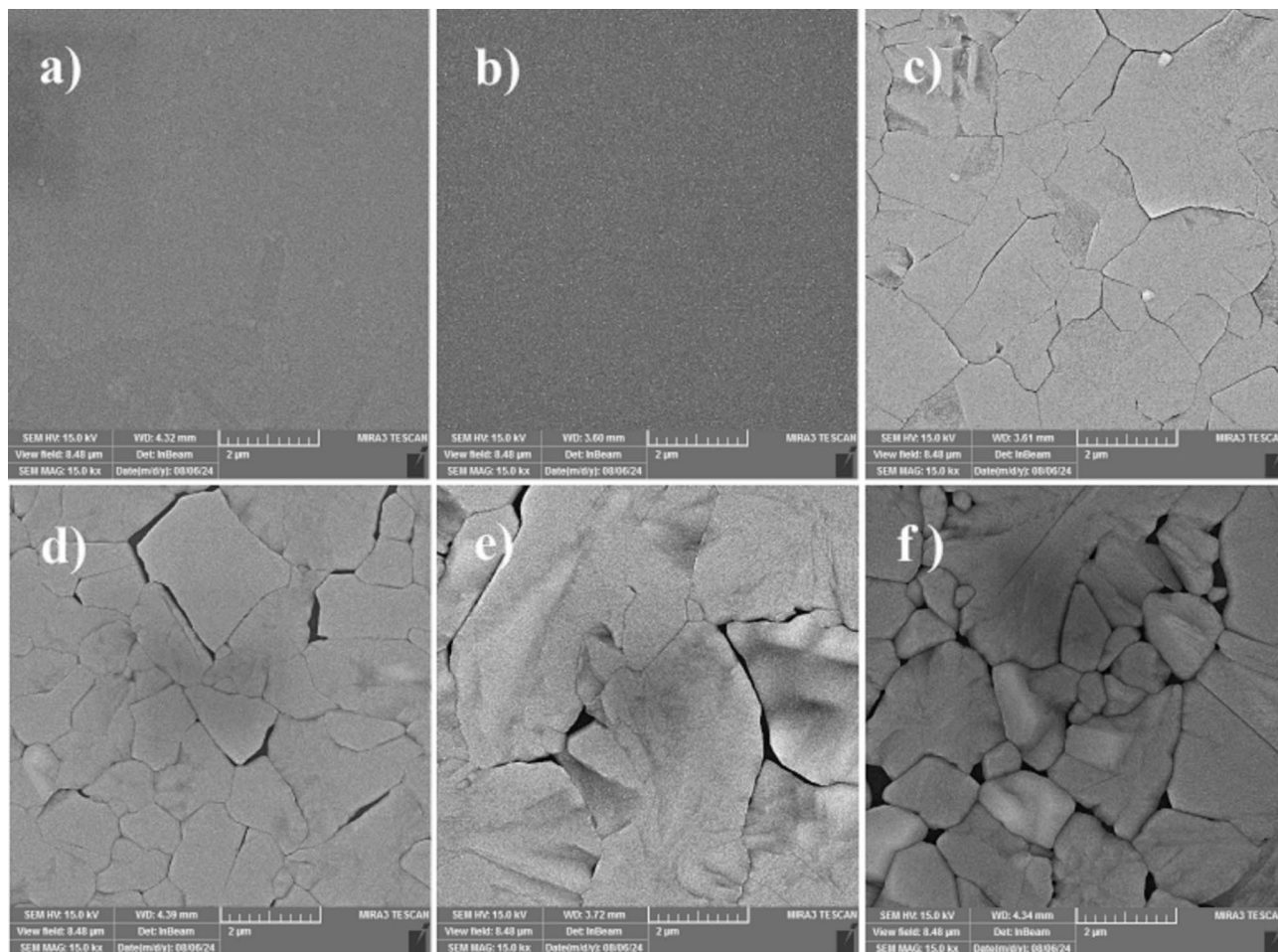
Fig. 3. FESEM images of annealed thin films: (**a**) Ta$_2$O$_5$, (**b**) WO$_3$, (**c**) Ta-WO$_3$ (I), (**d**) Ta-WO$_3$ (II), (**e**) Ta-WO$_3$ (III), and (**f**) Ta-WO$_3$ (IV).

reports suggested that the surface roughening of the photoanode films serves as an efficient method to optimize the photoelectrochemical response[80].

Structural analysis

The crystallographic properties of the synthesized thin films were investigated using XRD measurements. The XRD paterns of Ta$_2$O$_5$, WO$_3$, and Ta-doped WO$_3$ thin films annealed at 550 °C are shown in Fig. 6. For the Ta$_2$O$_5$ film, the absence of any diffraction peak confirmed its amorphous nature. The crystallization resistance was expected for the annealed Ta$_2$O$_5$ films in the temperature range of 300–700 °C as reported in the literature[81]. For undoped and Ta-doped WO$_3$ films, the detected XRD diffractions were consistent with the monoclinic phase of WO$_3$ (JCPDS No: 00-033-1387). The XRD peaks related to Ta–W-O or oxides of Ta were not found for Ta-doped WO$_3$ films. The well-resolved peaks at 23.23°, 24.41°, 34.1°, 41.88°, and 56.07° correspond to the (002), (200), (112), (022), (222), and (124) planes, respectively[82,83]. The presence of more peaks in the XRD pattern of Ta-doped WO$_3$ compared to undoped WO$_3$ indicates the formation of better crystalline WO$_3$ films after Ta doping. This result suggests that the transition to a crystalline phase occurs more easily for combined oxide of W and Ta than for pure Ta$_2$O$_5$ and WO$_3$. The strongest peak (200) of Ta-doped WO$_3$ films was analyzed to determine crystallite size by Debye–Scherrer relation[41]:

$$D = 0.9\lambda/\beta\cos\theta \qquad (1)$$

where λ is the X-ray wavelength (1.5418 A°), β is FWHM of (200) peak, and θ is the diffraction angle. With increasing RF sputtering power (10–60 W), a increase in crystallite size of Ta-doped WO$_3$ was found from 73.81 to 110.5 nm, as shown in Table 2. According to previous reports, the crystal plane orientation of WO$_3$ films significantly affects the water splitting efficiency. Li et al. reported that WO$_3$ doped with different concentrations (0–20 wt%) of Mg after sintering at 950 °C showed different crystallization behavior, which affected their photoelectrochemical performance. For example, a new phase (MgWO$_4$) was found for 10 wt% Mg-doped WO$_3$, which was neither MgO nor WO$_3$[49]. On the other hand, it has been reported that the incorporation of Ta or Ti ions into the WO$_3$ crystal lattice prepared by the hydrothermal method prevents the formation
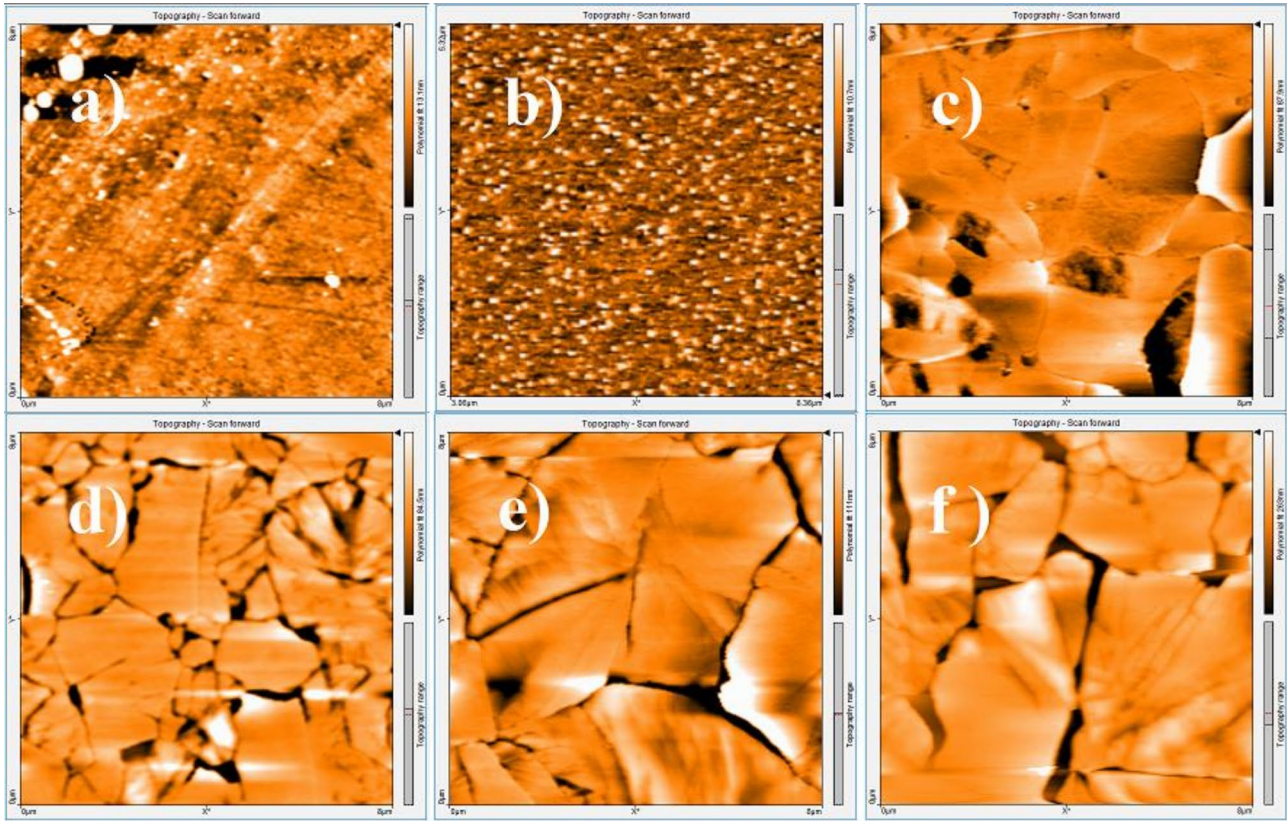
Fig. 4. AFM images of annealed thin films: (**a**) Ta_2O_5, (**b**) WO_3, (**c**) Ta-WO$_3$ (I), (**d**) Ta-WO$_3$ (II), (**e**) Ta-WO$_3$ (III), and (**f**) Ta-WO$_3$ (IV).

Thin film	σ_{rms} (nm)	Crystallite size (nm)	T_{av} (%)
Ta_2O_5	1.79	–	92.82
WO_3	1.98	–	90.01
Ta-WO$_3$ (I)	14.71	73.81	88.06
Ta-WO$_3$ (II)	16.04	74.86	84.80
Ta-WO$_3$ (III)	30.42	55.40	74.00
Ta-WO$_3$ (IV)	47.94	110.5	74.27

Table 2. Surface roughness, crystallite size, and average transmittance for sputter deposited thin films.

of a pure monoclinic phase after annealing at 500 °C, and multiple phases (hexagonal and monoclinic) are usually produced[64,84]. In the present study, the formation of a pure monoclinic phase, which is preferred for the water splitting reaction, was successful for Ta-doped WO$_3$ thin films deposited by magnetron co-sputtering after annealing at 500 °C. Recently, Wang et al. reported that WO$_3$ films grown with enriched the (002) plane by hydrothermal method enable more efficient water splitting reaction with remarkable photocurrent density[85]. In the present case, with increasing Ta concentration above 3.27 at%, a peak at 23.23° corresponding to (002) plane was noticed. In conclusion, Ta doping into WO$_3$ by promoting the growth of (002) direction can be helpful to enhance the water splitting performance. It is clear that increasing Ta consentration into WO$_3$ lattice leads to a gradual shift in the XRD peak positions of (222) and (124) planes towards higher 2θ value. This is attributed to the substitution of some W^{6+} ions by Ta atoms in the WO$_3$ crystal structure. When the radius of the substituting material is different from the host material, the occurrence of compressive strain in the crystal leads to the reduction of lattice parameters[60,84].

Optical properties

The bandgap nature and optical parameters of the synthesized thin films were examined by UV–Vis spectroscopic analysis in the wavelength range of 200–1100 nm. Figure 7 represents the transmittance spectra of Ta_2O_5, WO_3, and Ta-doped WO$_3$ thin films annealed at 550 °C. The existence of oscillatory modes in the spectra is due to the interference phenomenon caused by multiple reflections of light at the film-substrate interface[86]. The comparative analysis of the spectra exhibits that the optical behavior of Ta-doped WO$_3$ thin films strongly
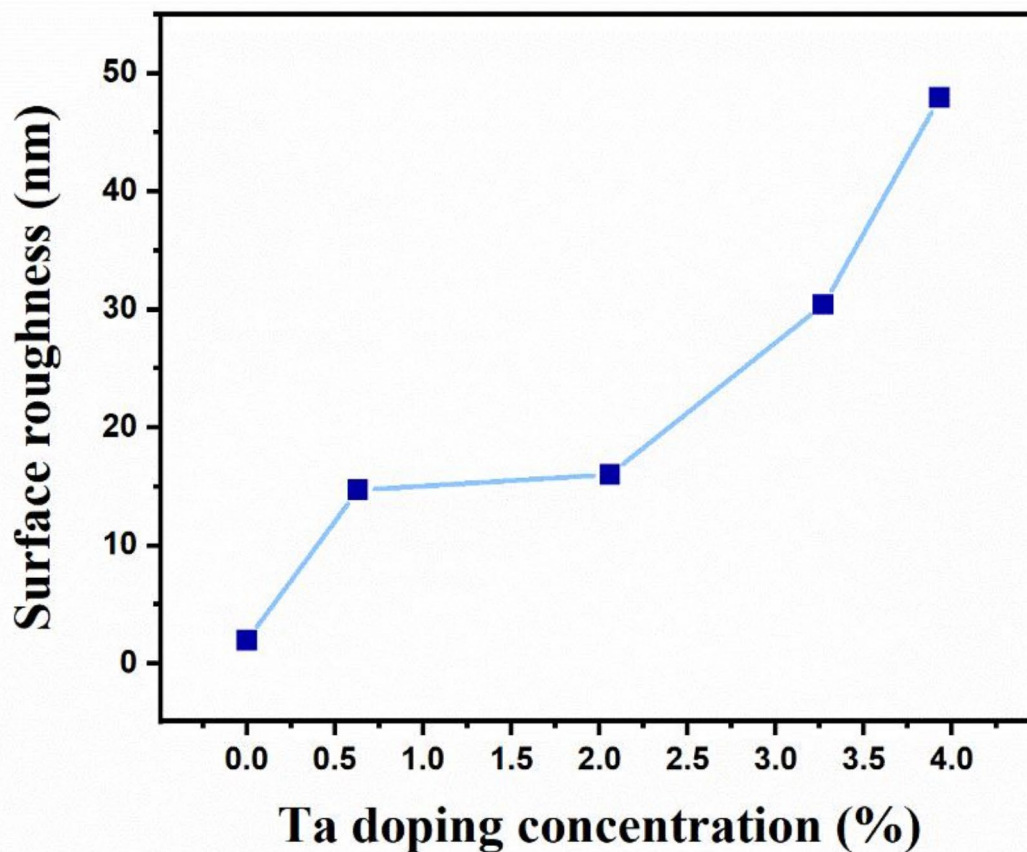
Fig. 5. variation of surface roughness as a function of Ta doping concentration.

depends on the Ta concentration. It is clear that the transparency of WO$_3$ films in the visible region decreases rapidly with increasing Ta concentration. The average transmittance (T$_{av}$) was calculated in the visible range ($\lambda = 380$–780 nm) using the following relation[87]:

$$T_{av} = \frac{\int V(\lambda) T(\lambda) d\lambda}{\int V(\lambda) d\lambda} \tag{2}$$

Here, V(λ) is the photopic luminous efficiency, representing the sensitivity of the standard observer for photometry[88]. The obtained values of T$_{av}$ for the prepared samples are listed in Table 2. Pure Ta$_2$O$_5$ films exhibit the highest T$_{av}$ value in the visible region. It was clear that the optical transparency of doped films decreases noticeably with increasing Ta concentration, as shown in Fig. 11. This can be explained by two reasons: Firstly, the intra-band excitation of charge carriers in the conduction band states leads to increased absorption as a result of reduced transmission[89,90]. Meanwhile, the reduction in T$_{av}$ with increasing Ta concentration can be associated with the enhanced light scattering caused by the improvement of crystallinity and the increase in surface roughness as evident from structural and morphological studies (XRD and AFM results)[91,92]. A sharp drop in the transmittance value between 300 and 400 nm corresponds to the fundamental absorption, indicating the semiconducting nature of the prepared films[93]. Figure 8 represents the absorbance spectra of the prepared thin films. A careful observation of the spectra exhibits the enhancement of absorption in the visible region with increasing Ta concentration into the WO$_3$ lattice. The fundamental absorption edge corresponds to the direct transition of an electron from the top of valence band to the bottom of conduction band, which can be employed to find the nature (direct or indirect) and value of the bandgap[94]. The optical absorption coefficient (α) is a necessary quantity to find the band gap energy of thin films, which can be determined using transmittance (T) and film thickness (d) as follows[75,95]:

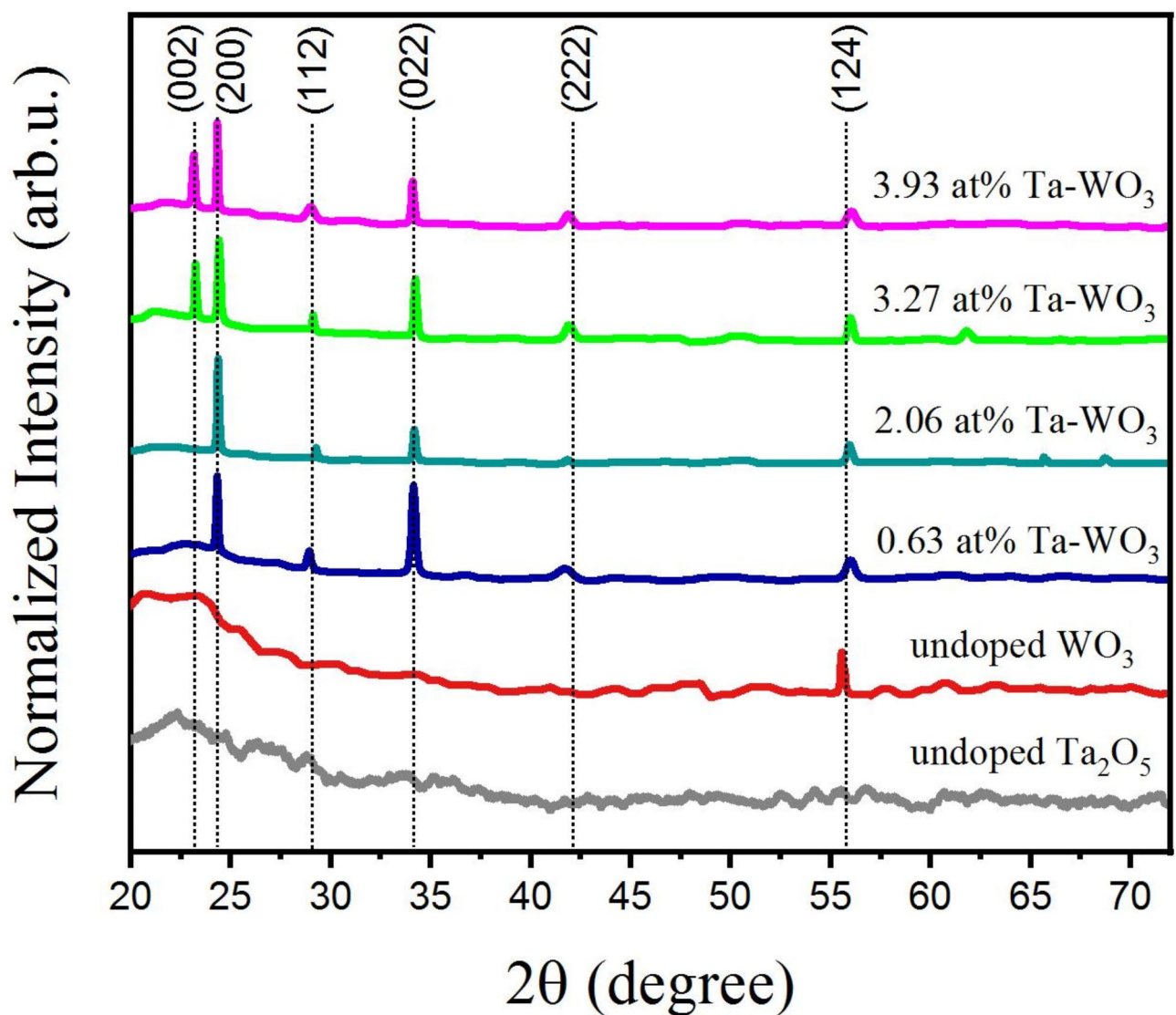$$\alpha = \frac{1}{d} \ln\left(\frac{1}{T}\right) \tag{3}$$

Fig. 6. XRD pattern of Ta_2O_5, WO_3, and Ta-doped WO_3 thin films with different dopant concentrations.

Figure 9 shows a sharp drop in α values in the UV spectral region and a relatively stabilized behavior in the visible light range. It is also found that the absorption coefficient of WO_3 films gradually increases with increasing Ta concentration, which results from enhanced absorption. A significant shift of the absorption edge towards longer wavelengths after Ta-doping leads to a reduction in the bandgap energy. The optical bandgap is an effective property to evaluate the photosensitivity of materials. The optical bandgap energy (E_g) of thin films can be extracted through the well-known Tauc relation[96]:

$$\alpha h\upsilon = B\left(h\upsilon - Eg\right)^m \tag{4}$$

Here, B is the band edge constant that depends on the crystalline quality, h is the Planck's constant, υ is the frequency of incident light, α is the absorption coefficient, and m is the power coefficient. The power coefficient is related to the nature of transition, which takes the values of 1/2, 2, 3/2, or 3 for direct allowed, indirect allowed, direct forbidden, and indirect forbidden electron transitions, respectively. Figure 10 depicts the Tauc plots for Ta_2O_5, WO_3, and Ta-doped WO_3 thin films annealed at 550 °C, considering the indirect allowed transition (n = 2). Extrapolation of the linear part of $(\alpha h\upsilon)^{1/2}$ until crossing the energy axis was used to estimate bandgap values[97]. The extracted E_g values for the Ta_2O_5, WO_3, and Ta-doped WO_3 thin films to be 4.00, 3.07, and 2.61–3.01 eV, respectively. Table 3 shows that the optical bandgaps of the prepared samples are very close to the results reported for these materials synthesized by other techniques. The decreasing trend of the optical bandgap of WO_3 films from 3.07 to 2.61 eV with increasing Ta concentration (0–3.93%) is depicted in Fig. 11. The narrowing of the bandgap and the enhancement of visible light absorption after Ta-doping can be attributed to the generation of localized impurity levels between the valence band (VB) and conduction band (CB) of WO_3. These levels serve as trapping states that allow for additional electron excitation from the VB to the impurity level or from the
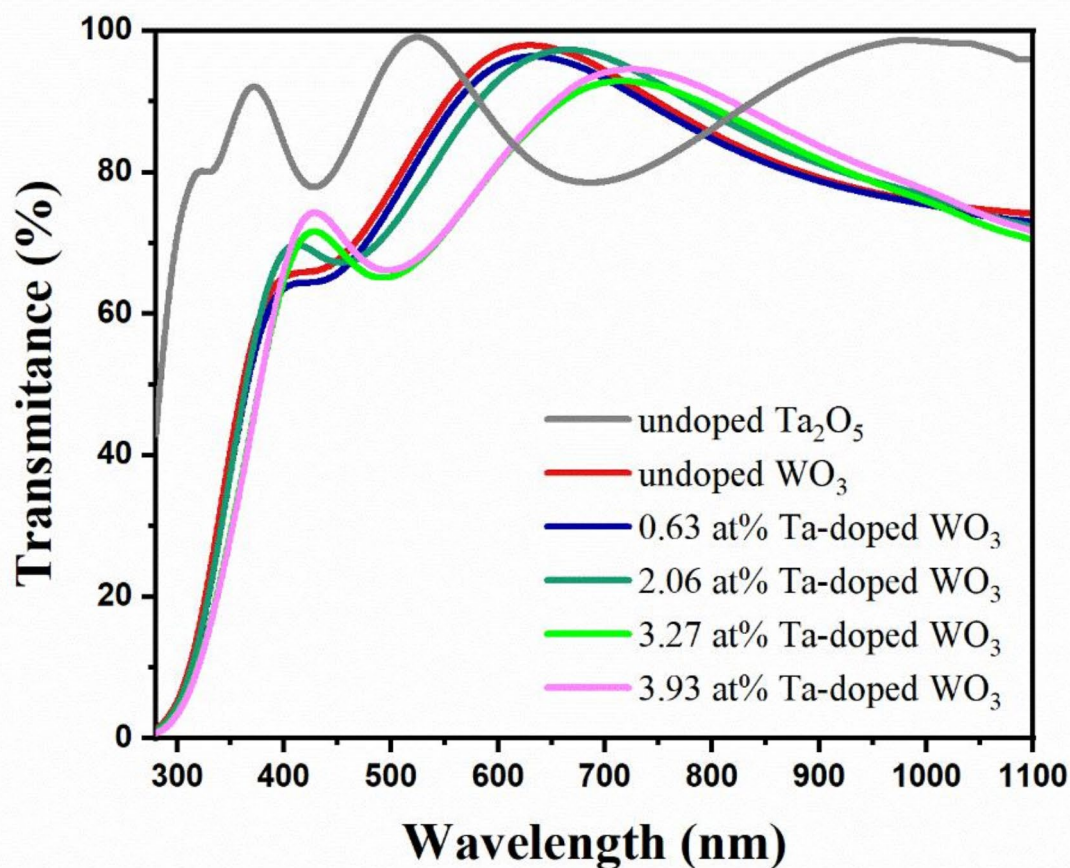
Fig. 7. Transmittance spectra of Ta_2O_5, WO_3, and Ta-doped WO_3 thin films with different dopant concentrations.

impurity level to the CB[91]. Several recent reports confirm the reduction of the bandgap energy of tungsten oxide after doping with metal ions[45,47,60,64,98]. The bandgap value of 2.61 eV ensures better absorption of the incident light and enables the appropriate use of Ta-doped WO_3 as a photoanode in PEC water splitting.

Photoelectrochemical characterization

To evaluate the photoelectrochemical performance of the prepared electrodes, photocurrent–voltage measurements were conducted in a three-electrode setup by linear sweep voltammetry (LSV) in 0.2 M Na_2SO_4 electrolyte under one sun illumination. Figure 12 displays the LSV plots for undoped and 3.93 at% Ta-doped WO_3 thin films in the potential range of -0.4-1.6 V versus Ag/AgCl. It is clear that both undoped and Ta-doped electrodes exhibit negligible photocurrent responses under dark conditions. For undoped WO_3 photoanode, the photocurrent of ~ 0.19 mA/cm^2 was found at 1 V (vs. Ag/AgCl) under 1-sun irradiation. The maximum photocurrent obtained for undoped WO_3 in the present study is relatively less compared to the values reported in the literature[60,84]. This is mainly associated with the material production process and the orientation of the crystal planes. According to previous studies, the water oxidation reaction occurs on the (002) plane more efficiently than on other planes of the monoclinic phase. Because the energy change required to realize the water oxidation reaction in this plane is 1.62 eV, which is much less than the energy of 1.49 eV required for the reaction on the (200) plane[85]. Here, the undoped tungsten oxide films, despite forming a monoclinic crystalline phase after annealing, do not have the desired (002) crystal plane for the water splitting reaction, resulting in low photocurrent. More importantly, the substitution doping of Ta into WO_3 leads to a significant increase in photocurrent density. The samples prepared with different Ta dopant concentrations (0–3.93 at%) were analyzed in detail. The WO_3 film doped with 3.93 at% Ta exhibited the maximum photocurrent density of ~ 0.65 mA/cm^2 at 1 V (vs. Ag/AgCl). This value was about 3.42 times greater than undoped tungsten oxide electrodes. In this study, the achived photocurrent values are in good agreement with the results reported for Ta-doped WO_3 synthesized using hydrothermal method by Kalanur et al.[64] This can be due to the growth of the (002) crystal plane and the decrease in the bandgap energy (absorption of a large part of the incident light)[110]. Morever, the photocurrent value mentioned above was found to be noticeably higher than result reported for Ta-doped WO_3
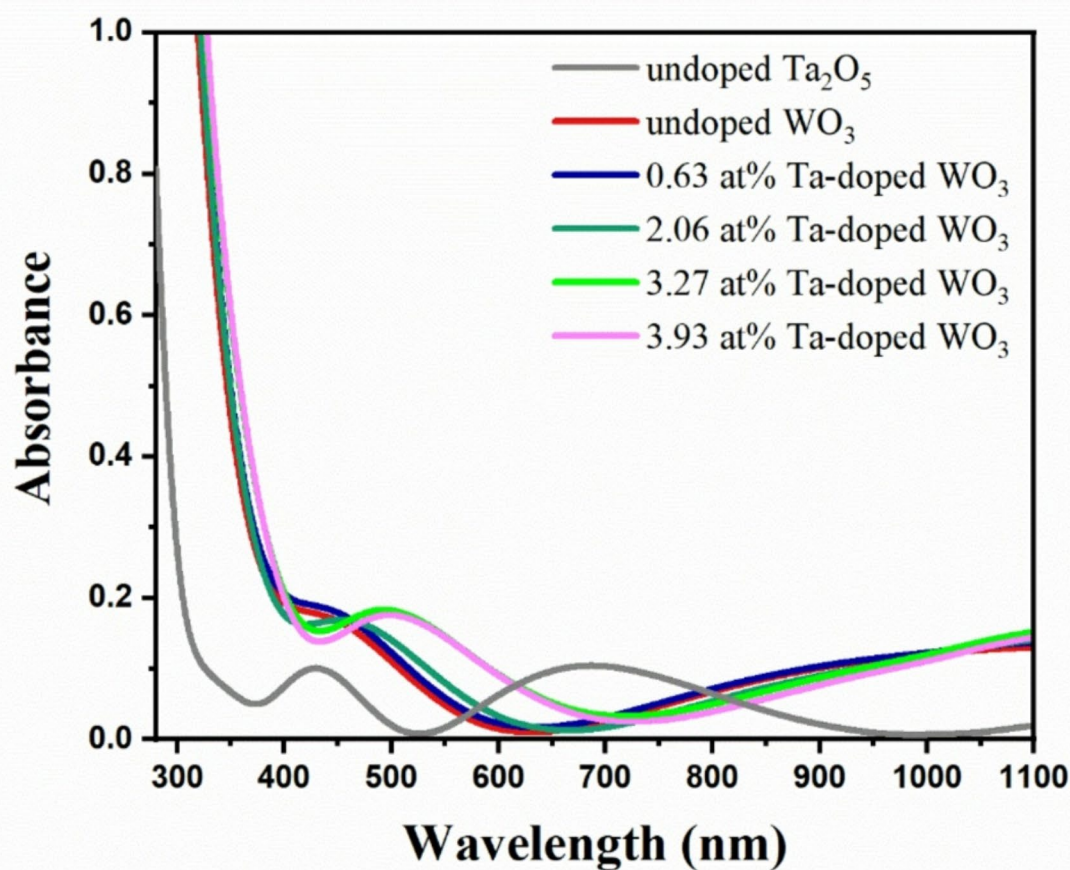
Fig. 8. Absorbance spectra of Ta_2O_5, WO_3, and Ta-doped WO_3 thin films with different dopant concentrations.

prepared via spray pyrolysis by Enesca et al.[111] This results indicate the the success of the sputtering method to synthesize thin films with desired properties. Similarly, Mohamed et al. reported photocurrent enhancement in TiO_xN_y/TiO_2 bilayer and nitrogen-doped TiO_2 films prepared by reactive dc magnetron sputtering method for application in PEC efficient water splitting. This phenomenon is due to the bandgap narrowing effect caused by nitrogen incorporation[112,113]. Comparatively, the photocurrent values obtained for sputter-deposited WO_3 and Ta-doped WO_3 films are listed in Table 4, along with previously reported results for WO_3 doped with various metals synthesized by different techniques. Overall water splitting activity was assessed using a two-electrode setup under on/off light illumination at 0 V bias. The measurements were carried out directly between the samples (working electrode) and the pt wire (counter electrode). Figure 13 depicts the dependency of photocurrent density on irradiation-time for undoped and Ta-doped WO_3 photoanodes. At the moment of illumination, a rapid increase in the photocurrent from zero to a certain value was observed for both undoped and doped samples. It is noticeable that the current density exhibited relatively stable trend during the period of light exposure and suddenly dropped to near zero at the moment of light extinction. Therefore, excellent photoresponsivity and slow electron–hole recombination are expected for WO_3 films doped with 3.93 at% Ta compared to undoped films[114]. On the other hand, the transient photocurrent (at 0 V) can be attributed to photogeneration of electron/hole pairs under light illumination. Finally, it can be concluded that the higher photocurrent of the Ta-doped electrodes is due to the increased electron/hole generation resulting from the narrowing of the optical bandgap.

Band edge positions

To realize the water splitting reaction on electrode materials, the production of charge carriers and redox potential are crucial parameters[98]. In the present work, the band structure of the prepared films is schematically discussed to evaluate the possible mechanism of the PEC reaction. The positions of valence band minimum (VBM) and conduction band maximum (CBM) for undoped and Ta-doped WO_3 samples were obtained by the following equations[115]:
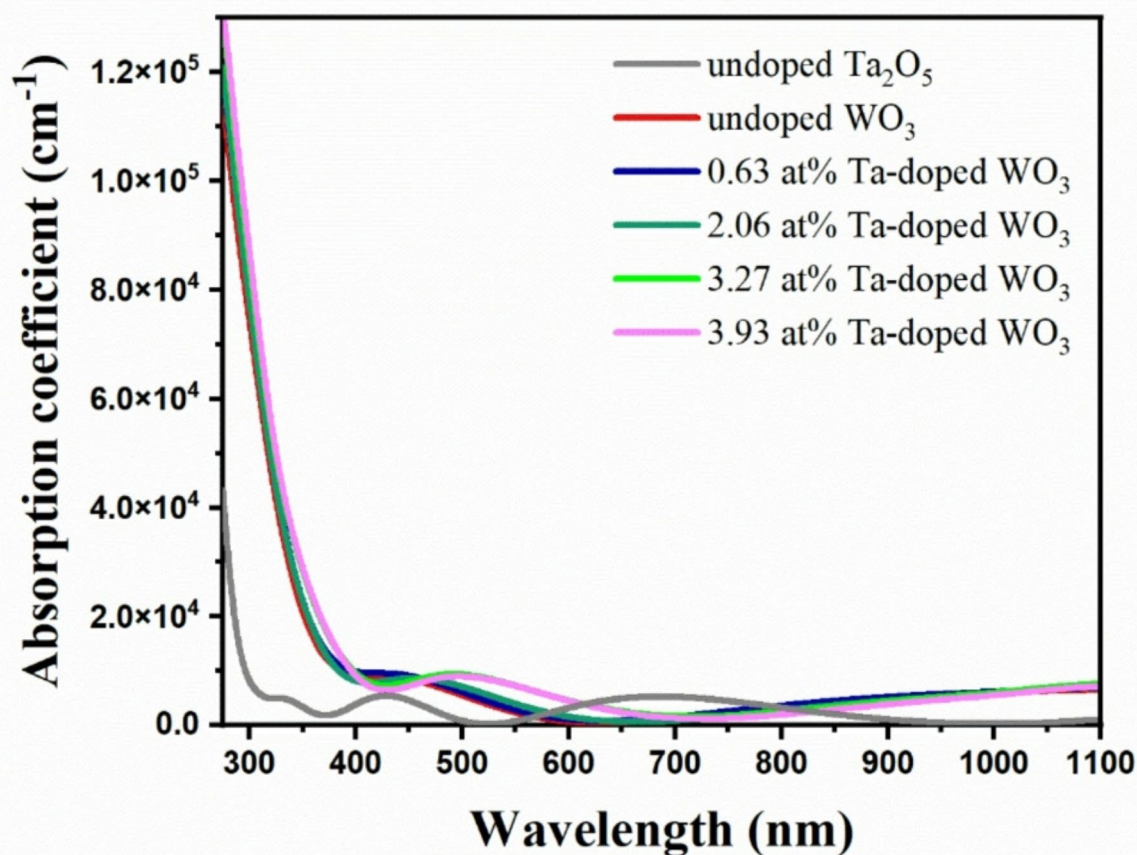
Fig. 9. Wavelength dependency of absorption coefficient for Ta_2O_5, WO_3, and Ta-doped WO_3 thin films with different dopant concentrations.

$$E_{CB} = X - E_e - \frac{1}{2}E_g \qquad (5)$$

$$E_{VB} = E_{CB} + E_g \qquad (6)$$

Here, E_{CB} represents the conduction band edge, X is the determined Mulliken electronegativity, E_e is the energy of the free electrons on the hydrogen scale (~4.5 eV), E_g is the bandgap energy estimated from Tauc plot, and E_{VB} is the valence band edge. Considering the above equation, the calculated E_{CB}/E_{VB} values of undoped and Ta-doped WO_3 samples are displayed in Fig. 14. Considering that the redox potential of H^+/H_2 is 0 eV, while the redox potential of O_2/H_2O is 1.23 eV. Consequently, the water splitting reaction theoretically requires a minimum bandgap of 1.23 eV, which refers to light with a wavelength of about 1100 nm. From the Fig. 14, it can be seen that the replacement of W with Ta in WO_3 leads to a downward shift in conduction band edge, an upward shift in valence band edge, and the significant reduction of the bandgap energy. This process occurs more noticeably with increasing Ta concentration.

Conclusion

In summary, this study reported the deposition of Ta-doped WO_3 thin films via reactive magnetron co-sputtering from W and Ta metal targets, and subsequent annealing at 550 °C. Tuning the elemental composition of Ta-doped WO_3 thin films by varying DC and RF sputtering powers allows narrowing of the band gap and altering of the band edge positions for use in PEC water splitting. By analyzing EDX results, it was concluded that the concentration of Ta dopant into WO_3 increased in the range of 0–3.93 at% with increasing RF sputtering power (0 to 60 W). From the FESEM and AFM micrographs, the growth of a granular structure and surface roughening were observed after Ta doping. Comparative studies of XRD patterns confirmed that the substitution of Ta atoms into the WO_3 structure during annealing improved the crystallinity, especially in the (002) direction. UV-Vis spectroscopic measurements showed that addition of Ta into WO_3 decreased the average transparency (from 92.82 to 74.27%), increased visible light absorption, and narrowed bandgap (from 3.07 to 2.61 eV). Linear sweep
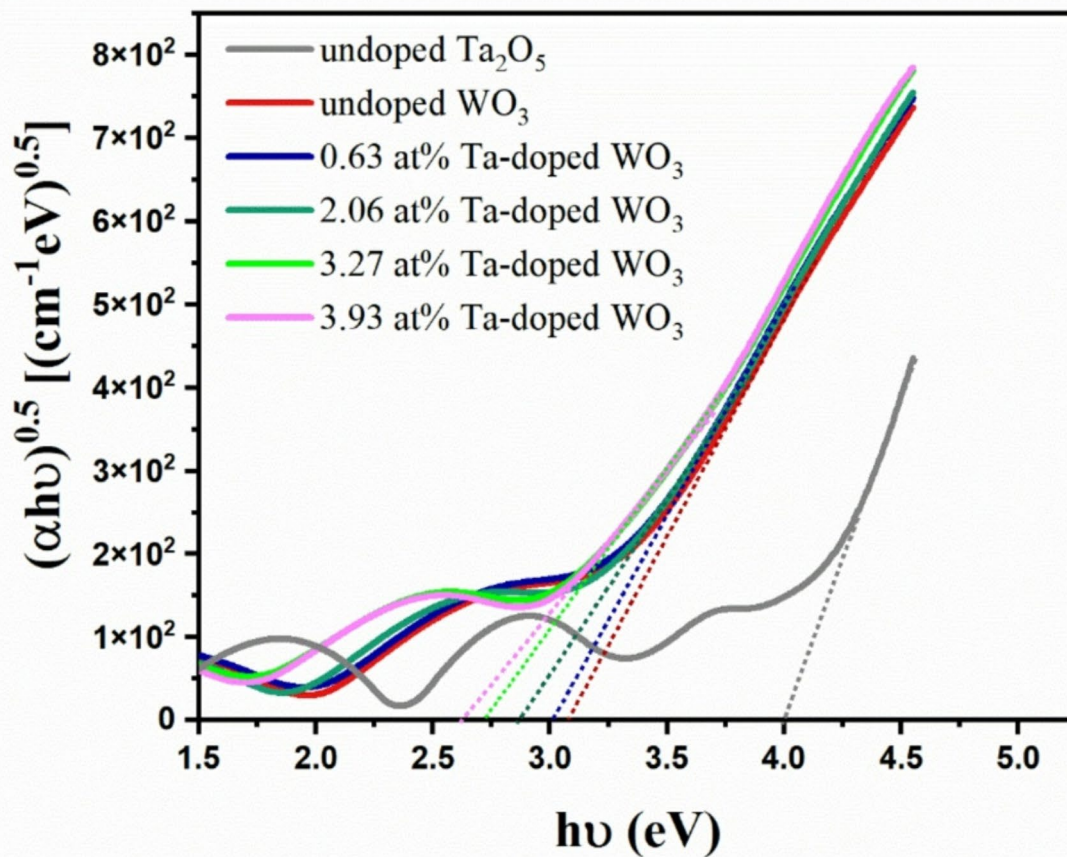
Fig. 10. Tauc plots for for Ta_2O_5, WO_3, and Ta-doped WO_3 thin films with different dopant concentrations.

Thin film	E_g (eV)	Deposition techniques	References
Ta_2O_5	4.00	RF magnetron sputtering	This work
	4.18	Pulsed laser deposition	99
	4.20	Atomic layer deposition	100
	4.47	DC magnetron sputtering	101
	4.2	Ion-beam sputtering	102
WO_3	3.07	DC magnetron sputtering	This work
	2.89–3.09	Impulse magnetron sputtering	103
	2.96–3.15	RF magnetron sputtering	104
	3.07	Pulsed dc magnetron sputtering	105
	2.90–3.18	DC magnetron sputtering	106
	3.00	Atomic layer deposition	82
	3.18	Chemical vapor deposition	107
	3.26	Evaporation–condensation	108
	3.20	Dual magnetron sputtering	109
Ta-doped WO_3	3.01–2.61	Magnetron co-sputtering	This work
	2.61	Hydrothermal	64
	3	RF magnetron sputtering	77

Table 3. Comparision of bandgap energy for Ta_2O_5, WO_3, and Ta-doped WO_3 thin films.
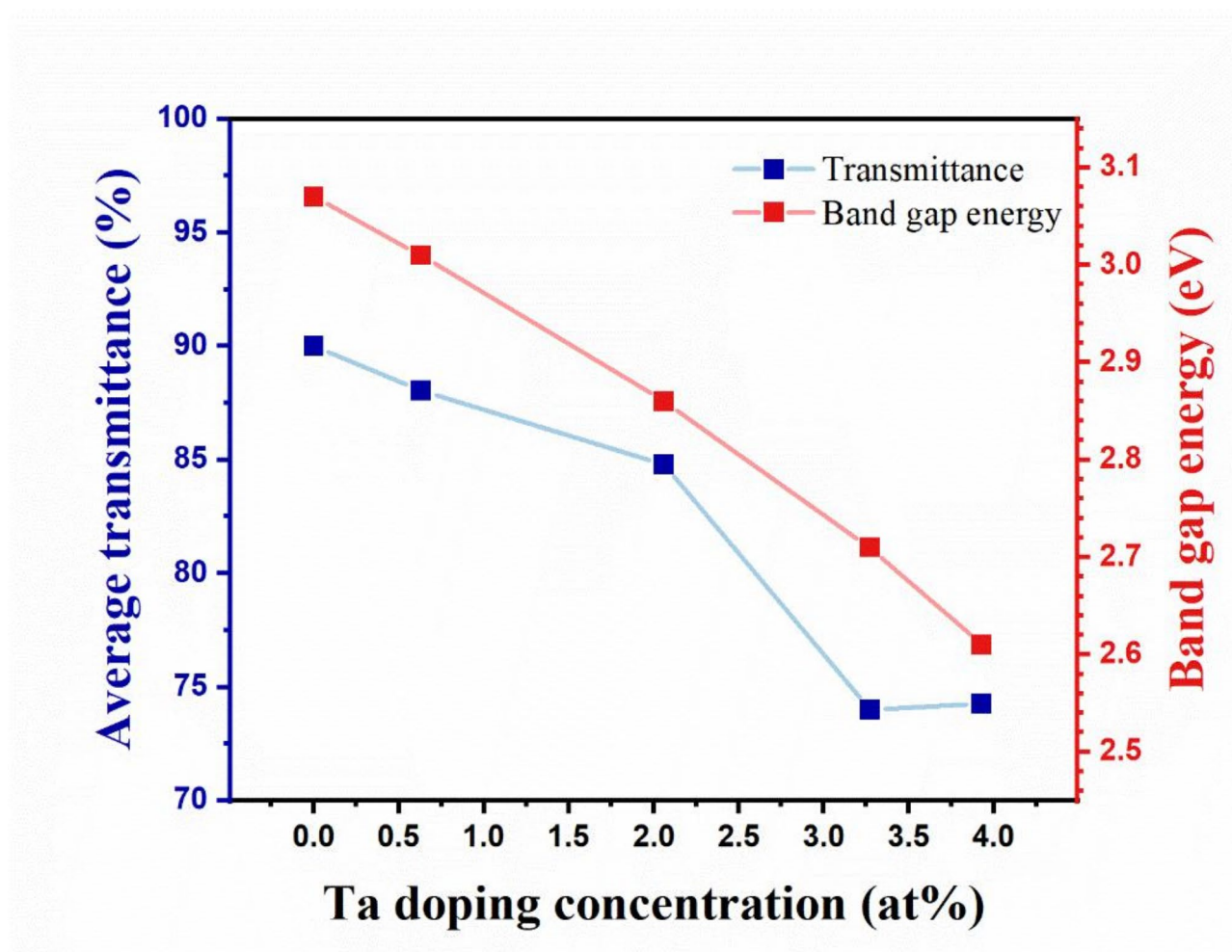
Fig. 11. variation of average transmittance and bandgap energy as a function of Ta dopant concentration.

voltammetry data showed that the photocurrent density of WO_3 increased from 0.19 mA/cm^2 to 0.65 mA/cm^2 (at 1 V vs. Ag/AgCl) after doping with 3.93 at% tantalum. The incorporation of Ta ions into WO_3 lattice shifted the valence band up and the conduction band down. Performed studies suggest that sputtered WO_3 thin films can be modified by Ta-doping combined with post-annealing for application in efficient photoelectrochemical water splitting.
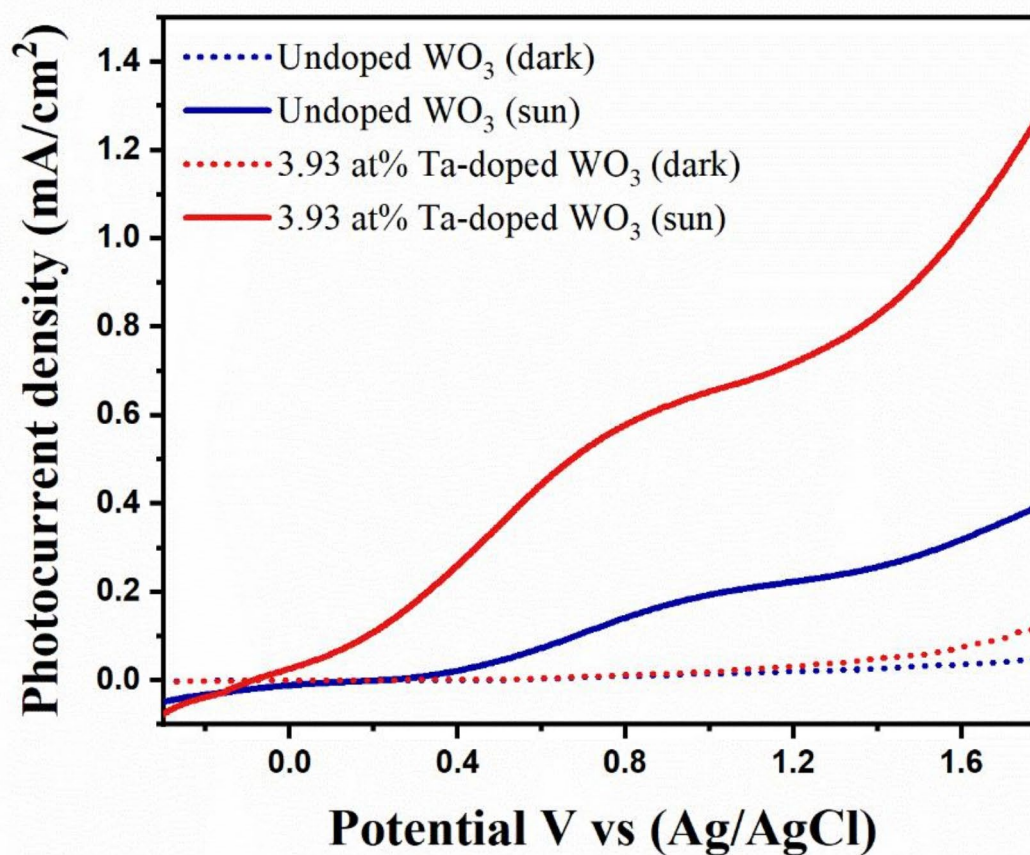
Fig. 12. Linear sweep voltammetry plots for undoped and Ta-doped WO$_3$.

Thin film	Photocurrent (mA/cm^2)	Measurement conditions	Deposition techniques	References
Ta-WO$_3$	0.65	1 V (vs. Ag/AgCl)	Co-sputtering	This work
Ta-WO$_3$	0.60	1.23 V (vs. RHE)	Hydrothermal	[64]
Gd-WO$_3$	1.49	1 V (vs. Ag/AgCl)	Hydrothermal	[63]
Nb-WO$_3$	0.414	1.23 V (vs. RHE)	Hydrothermal	[76]
Sn-WO$_3$	0.427	1.23 V (vs. RHE)	Hydrothermal	[60]
Ti-WO$_3$	1.139	1.23 V (vs. RHE)	Hydrothermal	[84]
V-WO$_3$	0.201	1.23 V (vs. RHE)	Hydrothermal	[47]
Cr-WO$_3$	0.024	1.23 V (vs. RHE)	Hydrothermal	[47]
Mn-WO$_3$	0.295	1.23 V (vs. RHE)	Hydrothermal	[47]
Fe-WO$_3$	0.442	1.23 V (vs. RHE)	Hydrothermal	[47]
Co-WO$_3$	0.636	1.23 V (vs. RHE)	Hydrothermal	[47]
Ni-WO$_3$	0.364	1.23 V (vs. RHE)	Hydrothermal	[47]
Cu-WO$_3$	0.487	1.23 V (vs. RHE)	Hydrothermal	[47]
Zn-WO$_3$	0.375	1.23 V (vs. RHE)	Hydrothermal	[47]

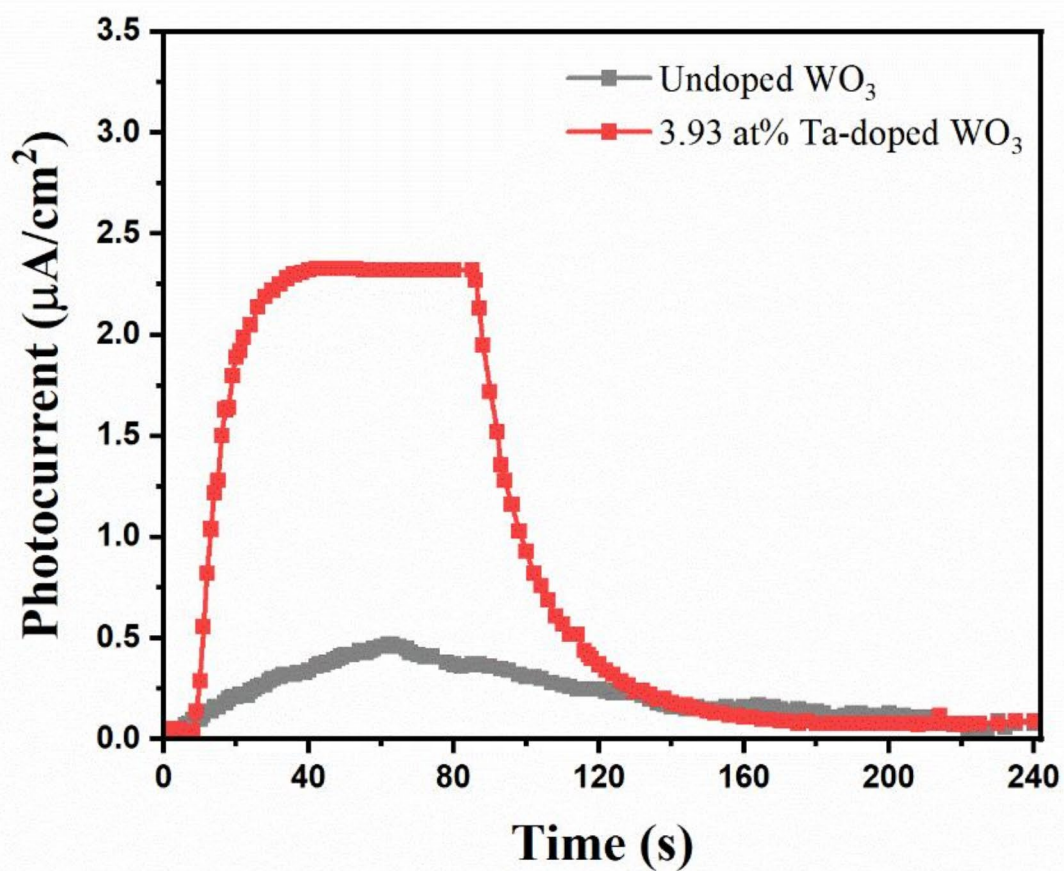**Table 4**. Comparision of photocurrent values for WO$_3$ thin films doped with various metals.

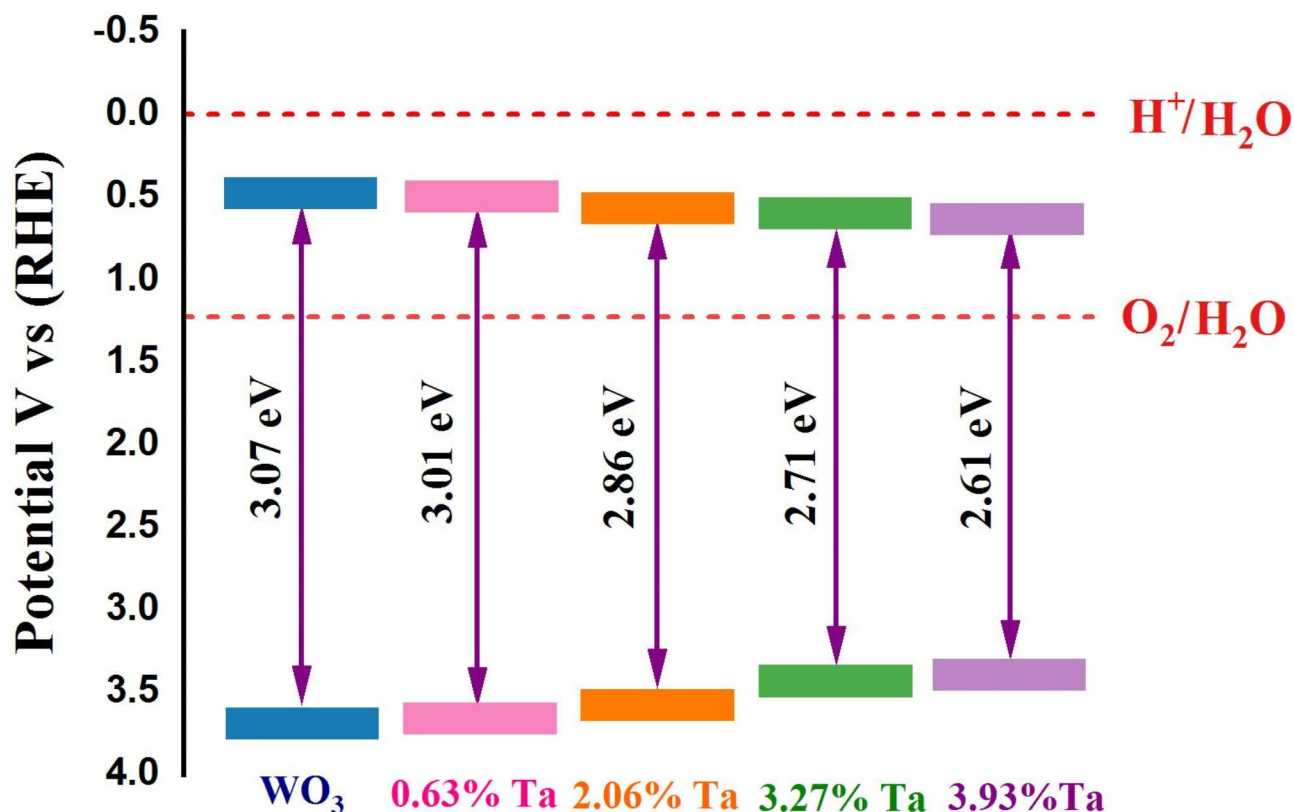**Fig. 13**. Time dependence of photocurrent at 0 V for undoped and Ta-doped WO_3.

Fig. 14. Schematic diagram of band positions for undoped and Ta-doped WO$_3$.

Data availability
Data is provided within the manuscript or supplementary information files. The datasets used and/or analysed during the current study available from the corresponding author on reasonable request.

References
1. Lewis, N. S. Research opportunities to advance solar energy utilization. *Science* **351**, 1920 (2016).
2. Tee, S. Y. et al. Recent progress in energy-driven water splitting. *Adv. Sci.* **4**, 1600337 (2017).
3. Manoharan, Y. et al. Hydrogen fuel cell vehicles; current status and future prospect. *Appl. Sci.* **9**, 2296 (2019).
4. Kalanur, S. S., Duy, L. T. & Seo, H. Recent progress in photoelectrochemical water splitting activity of WO$_3$ photoanodes. *Topics Catal.* **61**, 1043–1076 (2018).
5. Kudo, A. & Miseki, Y. Heterogeneous photocatalyst materials for water splitting. *Chem. Soc. Rev.* **38**, 253–278 (2009).
6. Hisatomi, T. & Domen, K. Reaction systems for solar hydrogen production via water splitting with particulate semiconductor photocatalysts. *Nat. Catal.* **2**, 387–399 (2019).
7. Kim, J. Y. et al. Single-crystalline, wormlike hematite photoanodes for efficient solar water splitting. *Sci. Rep.* **3**, 2681 (2013).
8. Song, H., Luo, S., Huang, H., Deng, B. & Ye, J. Solar-driven hydrogen production: Recent advances, challenges, and future perspectives. *ACS Energy Lett.* **7**, 1043–1065 (2022).
9. Preethi, L., Antony, R. P., Mathews, T., Walczak, L. & Gopinath, C. S. A study on doped heterojunctions in TiO$_2$ nanotubes: An efficient photocatalyst for solar water splitting. *Sci. Rep.* **7**, 14314 (2017).
10. Fujishima, A. & Honda, K. Electrochemical photolysis of water at a semiconductor electrode. *Nature* **238**, 37–38 (1972).
11. Li, W. et al. WO$_3$ nanoflakes for enhanced photoelectrochemical conversion. *ACS Nano* **8**, 11770–11777 (2014).
12. Kalanur, S. S., Yoo, I.-H., Park, J. & Seo, H. Insights into the electronic bands of WO$_3$/BiVO$_4$/TiO$_2$, revealing high solar water splitting efficiency. *J. Mater. Chem. A* **5**, 1455–1461 (2017).
13. Azmayesh, R., Naghshara, H., Aref, S. M., Ghafouri, M. & Siahsahlan, M. The effect of GO content on the improvement of efficient water splitting applications in ZnO/GO nanocomposites. *Int. J. Hydrog. Energy* **84**, 511–520 (2024).
14. Azmayesh, R., Naghshara, H., Mohammadi Aref, S. & Ghafouri, M. Preparation of a polyaniline/ZnO-NPs composite for the visible-light-driven hydrogen generation. *Sci. Rep.* **14**, 3165 (2024).
15. Siahsahlan, M., Aref, S. M. & Naghshara, H. Structural and optical properties of ZnO thin films as a function of pH value and its effect on photoelectrochemical water splitting. *Phys. Scr.* **99**, 055533 (2024).
16. Becker, J. P. et al. Modeling and practical realization of thin film silicon-based integrated solar water splitting devices. *Phys. Status Solidi (a)* **213**, 1738–1746 (2016).
17. Wang, G. et al. Hydrogen-treated TiO$_2$ nanowire arrays for photoelectrochemical water splitting. *Nano Lett.* **11**, 3026–3033 (2011).
18. Kang, Z. et al. Interface engineering for modulation of charge carrier behavior in ZnO photoelectrochemical water splitting. *Adv. Funct. Mater.* **29**, 1808032 (2019).

19. Hu, C., Chu, K., Zhao, Y. & Teoh, W. Y. Efficient photoelectrochemical water splitting over anodized p-type NiO porous films. *ACS Appl. Mater. Interfaces* **6**, 18558–18568 (2014).
20. Chai, X. et al. 3D ordered urchin-like TiO_2@ Fe_2O_3 arrays photoanode for efficient photoelectrochemical water splitting. *Appl. Surf. Sci.* **470**, 668–676 (2019).
21. Luo, J. et al. Cu_2O nanowire photocathodes for efficient and durable solar water splitting. *Nano Lett.* **16**, 1848–1857 (2016).
22. Hadia, N. et al. Converting sewage water into H_2 fuel gas using Cu/CuO nanoporous photocatalytic electrodes. *Materials* **15**, 1489 (2022).
23. Paul, M. J. et al. $CuO–La_2O_3$ composite-enabled MIS Schottky barrier diodes: A novel approach to optoelectronic device diversification. *J. Inorg. Organomet. Polym. Mater.* **35**, 1–13 (2024).
24. Gayathri, P. et al. Enhancing photovoltaic applications through precipitating agents in ITO/CIS/CeO_2/Al heterojunction solar cell. *Inorg. Chem. Commun.* **168**, 112866 (2024).
25. Zhang, Z. et al. Toward efficient photoelectrochemical water-splitting by using screw-like SnO_2 nanostructures as photoanode after being decorated with CdS quantum dots. *Nano Energy* **19**, 318–327 (2016).
26. Ko, T.-R., Chueh, Y.-C., Lai, Y.-H. & Lin, C.-Y. Simultaneous enhancement in charge separation and interfacial charge transfer of BiVO4 photoanode for photoelectrochemical water oxidation. *J. Taiwan Inst. Chem. Eng.* **111**, 80–89 (2020).
27. Yamakata, A., Ishibashi, T.-A., Kato, H., Kudo, A. & Onishi, H. Photodynamics of $NaTaO_3$ catalysts for efficient water splitting. *J. Phys. Chem. B* **107**, 14383–14387 (2003).
28. Wang, G. et al. Bandgap engineering of KTaO3 for water-splitting by different doping strategies. *Int. J. Hydrog. Energy* **46**, 38663–38677 (2021).
29. Sharma, D. et al. Improved photoelectrochemical water splitting performance of Cu_2O/$SrTiO_3$ heterojunction photoelectrode. *J. Phys. Chem. C* **118**, 25320–25329 (2014).
30. Read, C. G., Park, Y. & Choi, K.-S. Electrochemical synthesis of p-type $CuFeO_2$ electrodes for use in a photoelectrochemical cell. *J. Phys. Chem. Lett.* **3**, 1872–1876 (2012).
31. Tijare, S. N. et al. Photocatalytic hydrogen generation through water splitting on nano-crystalline $LaFeO_3$ perovskite. *Int. J. Hydrog. Energy* **37**, 10451–10456 (2012).
32. Berglund, S. P. et al. Comprehensive evaluation of $CuBi_2O_4$ as a photocathode material for photoelectrochemical water splitting. *Chem. Mater.* **28**, 4231–4242 (2016).
33. Ozer, Z. N., Ozkan, M. & Pat, S. Investigation of the microstructural, surface, and optical properties of WO_3-doped ZnO thin films. *Inorg. Chem. Commun.* **170**, 113301 (2024).
34. Hassaballa, S. et al. WN_xO_y prepared by oxidation of tungsten nitride as alternative for the sputtered N doped WO_3 photocatalyst. *J. Mater. Sci. Mater. Electron.* **35**, 29 (2024).
35. Mindil, A., Mohamed, S., Alsubaie, A. S. & Rabia, M. WO_3/Cu_2O–CuO and WO_3/Au/Cu_2O–CuO heterojunctions photocatalysts for self-cleaning and photocatalytic degradation of organic pollutants applications. *Phys. Scr.* **99**, 105964 (2024).
36. Sibu, G. A., Gayathri, P., Akila, T., Marnadu, R. & Balasubramani, V. Manifestation on the choice of a suitable combination of MIS for proficient Schottky diodes for optoelectronic applications: A comprehensive review. *Nano Energy* **125**, 109534 (2024).
37. Akila, T. et al. Augmented photovoltaic performance of Cu/Ce–Sn: Cd)/n-Si Schottky barrier diode utilizing dual-doped Ce–(Sn: Cd) thin films. *Opt. Mater.* **149**, 115133 (2024).
38. Liu, R. et al. Water splitting by tungsten oxide prepared by atomic layer deposition and decorated with an oxygen-evolving catalyst. *Angew. Chem. Int. Ed* **50**, 499–502 (2011).
39. Zhu, T., Chong, M. N. & Chan, E. S. Nanostructured tungsten trioxide thin films synthesized for photoelectrocatalytic water oxidation: A review. *ChemSusChem* **7**, 2974–2997 (2014).
40. Wang, G. et al. Hydrogen-treated WO_3 nanoflakes show enhanced photostability. *Energy Environ. Sci.* **5**, 6180–6187 (2012).
41. Jafarpour, S., Naghshara, H. & Parhizkar, M. The effect of DC power and annealing on the structural, optical, and electrical characteristics of sputtered amorphous WO_x thin films. *Mater. Chem. Phys.* **313**, 128637 (2024).
42. Hodes, G., Cahen, D. & Manassen, J. Tungsten trioxide as a photoanode for a photoelectrochemical cell (PEC). *Nature* **260**, 312–313 (1976).
43. Joy, J., Mathew, J. & George, S. C. Nanomaterials for photoelectrochemical water splitting: Review. *Int. J. Hydrog. Energy* **43**, 4804–4817 (2018).
44. Liu, X., Wang, F. & Wang, Q. Nanostructure-based WO_3 photoanodes for photoelectrochemical water splitting. *Phys. Chem. Chem. Phys.* **14**, 7894–7911 (2012).
45. Kalanur, S. S. & Seo, H. Influence of molybdenum doping on the structural, optical and electronic properties of WO_3 for improved solar water splitting. *J. Colloid Interface Sci.* **509**, 440–447 (2018).
46. Wang, F., Di Valentin, C. & Pacchioni, G. Doping of WO_3 for photocatalytic water splitting: hints from density functional theory. *J. Phys. Chem. C* **116**, 8901–8909 (2012).
47. Kalanur, S. S., Noh, Y.-G. & Seo, H. Engineering band edge properties of WO_3 with respect to photoelectrochemical water splitting potentials via a generalized doping protocol of first-row transition metal ions. *Appl. Surf. Sci.* **509**, 145253 (2020).
48. Wang, F., Di Valentin, C. & Pacchioni, G. Rational band gap engineering of WO_3 photocatalyst for visible light water splitting. *ChemCatChem* **4**, 476 (2012).
49. Hwang, D. W., Kim, J., Park, T. J. & Lee, J. S. Mg-doped WO_3 as a novel photocatalyst for visible light-induced water splitting. *Catal. Lett.* **80**, 53–57 (2002).
50. Jalali, R., Parhizkar, M., Bidadi, H. & Naghshara, H. Correlation between optical, structural and microstructural properties of Ti–W–N thin films. *Ceram. Int.* **46**, 6454–6461 (2020).
51. Pat, S., Mohammadigharehbagh, R., Ozgur, N. A., Oztetik, B. & Korkmaz, S. Deep understanding in physical and electrochemical performance of WO3–TiO_2 nanocomposite thin films deposited onto ITO and FTO coated glass substrates using a thermionic vacuum arc deposition system. *Phys. B: Condens. Matter* **640**, 414093 (2022).
52. Wu, H. et al. Cathodic shift of onset potential for water oxidation of WO3 photoanode by Zr+ ions implantation. *J. Appl. Phys.* **121**, 8 (2017).
53. Maryam, I., Iqbal, T., Afsheen, S. & Ali, A. M. Synthesis and characterization of ta-doped WO_3 nanomaterials for their application as an efficient photocatalyst. *J. Inorg. Organomet. Polym. Mater.* **33**, 3454–3467 (2023).
54. Spetter, D. et al. Solvothermal synthesis of molybdenum–tungsten oxides and their application for photoelectrochemical water splitting. *ACS Sustain. Chem. Eng.* **6**, 12641–12649 (2018).
55. Song, H. et al. Synthesis of Fe-doped WO_3 nanostructures with high visible-light-driven photocatalytic activities. *Appl. Catal. B: Environ.* **166**, 112–120 (2015).
56. Hameed, A., Gondal, M. & Yamani, Z. Effect of transition metal doping on photocatalytic activity of WO_3 for water splitting under laser illumination: Role of 3d-orbitals. *Catal. Commun.* **5**, 715–719 (2004).
57. Ma, Y. & Hu, Y. H. Surface-copper-doped WO_3 photoanode for photoelectrochemical water splitting. *Appl. Phys. Lett.* **118**, 22 (2021).
58. Li, W. et al. Enhancing photoelectrochemical water splitting by aluminum-doped plate-like WO_3 electrodes. *Electrochim. Acta* **160**, 57–63 (2015).
59. Ng, K. H., Minggu, L. J. & Kassim, M. B. Gallium-doped tungsten trioxide thin film photoelectrodes for photoelectrochemical water splitting. *Int. J. Hydrog. Energy* **38**, 9585–9591 (2013).

60. Kalanur, S. S. Structural, optical, band edge and enhanced photoelectrochemical water splitting properties of tin-doped WO_3. *Catalysts* **9**, 456 (2019).
61. Kalanur, S. S., Yoo, I.-H., Eom, K. & Seo, H. Enhancement of photoelectrochemical water splitting response of WO_3 by Means of Bi doping. *J. Catal.* **357**, 127–137 (2018).
62. Yang, B. & Luca, V. Enhanced long-wavelength transient photoresponsiveness of WO 3 induced by tellurium doping. *Chem. Commun.*, 4454–4456 (2008).
63. Liu, Y. et al. Enhancement of the photoelectrochemical performance of WO_3 vertical arrays film for solar water splitting by gadolinium doping. *J. Phys. Chem. C* **119**, 14834–14842 (2015).
64. Kalanur, S. S. & Seo, H. Aligned nanotriangles of tantalum doped tungsten oxide for improved photoelectrochemical water splitting. *J. Alloys Compd.* **785**, 1097–1105 (2019).
65. Han, S. et al. Enhancing photoelectrochemical activity of nanocrystalline WO_3 electrodes by surface tuning with Fe(III). *Int. J. Hydrog. Energy* **37**, 16810–16816 (2012).
66. Özkan, E. & Tepehan, F. Optical and structural characteristics of sol–gel-deposited tungsten oxide and vanadium-doped tungsten oxide films. *Solar Energy Mater. Solar Cells* **68**, 265–277 (2001).
67. Shen, P., Syed-Bokhari, J. & Tseung, A. The performance of electrochromic tungsten trioxide films doped with cobalt or nickel. *J. Electrochem. Soc.* **138**, 2778 (1991).
68. Bathe, S. R. & Patil, P. Influence of Nb doping on the electrochromic properties of WO_3 films. *J. Phys. D: Appl. Phys.* **40**, 7423 (2007).
69. Tesfamichael, T., Ponzoni, A., Ahsan, M. & Faglia, G. Gas sensing characteristics of Fe-doped tungsten oxide thin films. *Sens. Actuators B: Chem.* **168**, 345–353 (2012).
70. Ahsan, M., Tesfamichael, T., Ionescu, M., Bell, J. & Motta, N. Low temperature CO sensitive nanostructured WO_3 thin films doped with Fe. *Sens. Actuators B: Chem.* **162**, 14–21 (2012).
71. Tesfamichael, T., Piloto, C., Arita, M. & Bell, J. Fabrication of Fe-doped WO_3 films for NO_2 sensing at lower operating temperature. *Sens. and Actuators B: Chem.* **221**, 393–400 (2015).
72. Jafarpour, S., Naghshara, H. & Aslibeiki, B. Structural, optical, and dielectric properties of ion-conducting $LiAlO_2$ thin films produced by reactive magnetron co-sputtering. *ACS Appl. Electron. Mater.* **5**, 1566–1574 (2023).
73. Jafarpour, S., Naghshara, H. & Aslibeiki, B. Correlation of sputtering power with microstructure and ionic conductivity in lithium aluminum oxide thin films prepared by reactive co-sputtering. *Ceram. Int.* **50**, 5665–5675 (2024).
74. Jalali, R., Parhizkar, M., Bidadi, H., Naghshara, H. & Eshraghi, M. J. Characterization of nano-crystalline Ti–W–N thin films for diffusion barrier application: A structural, microstructural, morphological and mechanical study. *Appl. Phys. A* **124**, 1–11 (2018).
75. Ekem, N. et al. Some physical properties of ZnO thin films prepared by RF sputtering technique. *Int. J. Hydrog. Energy* **34**, 5218–5222 (2009).
76. Kalanur, S. S., Yoo, I.-H., Cho, I. S. & Seo, H. Niobium incorporated WO3 nanotriangles: Band edge insights and improved photoelectrochemical water splitting activity. *Ceram. Int.* **45**, 8157–8165 (2019).
77. Kavitha, V., Suresh, S., Chalana, S. & Pillai, V. M. Luminescent Ta doped WO_3 thin films as a probable candidate for excitonic solar cell applications. *Appl. Surf. Sci.* **466**, 289–300 (2019).
78. Zare, M. et al. Evolution of rough-surface geometry and crystalline structures of aligned TiO_2 nanotubes for photoelectrochemical water splitting. *Sci. Rep.* **8**, 10870 (2018).
79. Memar, A., Daud, W. R. W., Hosseini, S., Eftekhari, E. & Minggu, L. J. Study on photocurrent of bilayers photoanodes using different combination of WO_3 and Fe_2O_3. *Solar Energy* **84**, 1538–1544 (2010).
80. Ibadurrohman, M. & Hellgardt, K. Importance of surface roughness of TiO_2 photoanodes in promoting photoelectrochemical activities with and without sacrificial agent. *Thin Solid Films* **705**, 138009 (2020).
81. Ren, W. et al. Annealing effects on the optical and electrochemical properties of tantalum pentoxide films. *J. Adv. Ceram.* **10**, 704–713 (2021).
82. Zhao, Y. et al. Physical and chemical defects in WO_3 thin films and their impact on photoelectrochemical water splitting. *ACS Appl. Energy Mater.* **1**, 5887–5895 (2018).
83. Mohamedkhair, A. K., Drmosh, Q. A., Qamar, M. & Yamani, Z. H. Tuning structural properties of WO_3 thin films for photoelectrocatalytic water oxidation. *Catalysts* **11**, 381 (2021).
84. Kalanur, S. S., Yoo, I.-H. & Seo, H. Fundamental investigation of Ti doped WO_3 photoanode and their influence on photoelectrochemical water splitting activity. *Electrochim. Acta* **254**, 348–357 (2017).
85. Wang, S. et al. Synergistic crystal facet engineering and structural control of WO_3 films exhibiting unprecedented photoelectrochemical performance. *Nano Energy* **24**, 94–102 (2016).
86. Gürakar, S., Ot, H., Horzum, S. & Serin, T. Variation of structural and optical properties of TiO_2 films prepared by DC magnetron sputtering method with annealing temperature. *Mater. Sci. Eng.: B* **262**, 114782 (2020).
87. Yu, S. et al. Fabrication of p-type SnO_2 films via pulsed laser deposition method by using Sb as dopant. *Appl. Surf. Sci.* **286**, 417–420 (2013).
88. Driscoll, W. G. & Vaughan, W. Handbook of optics sponsored by the Optical Society of America. In *Handbook of Optics Sponsored by the Optical Society of America New York* (1978).
89. Montero, J., Herrero, J. & Guillén, C. Preparation of reactively sputtered Sb-doped SnO_2 thin films: Structural, electrical and optical properties. *Solar Energy Mater. Solar Cells* **94**, 612–616 (2010).
90. Al-Kuhaili, M. Co-sputtered tantalum-doped tin oxide thin films for transparent conducting applications. *Mater. Chem. Phys.* **257**, 123749 (2021).
91. Sun, Z. et al. Effect of nitrogen-doping and post annealing on wettability and band gap energy of TiO_2 thin film. *Appl. Surf. Sci.* **500**, 144048 (2020).
92. Korpi, A. G. et al. Influence of the oxygen partial pressure on the growth and optical properties of RF-sputtered anatase TiO_2 thin films. *Results Phys.* **7**, 3349–3352 (2017).
93. Mahjabin, S. et al. Effects of oxygen concentration variation on the structural and optical properties of reactive sputtered WO_x thin film. *Solar Energy* **222**, 202–211 (2021).
94. Nair, P. B. et al. Effect of RF power and sputtering pressure on the structural and optical properties of TiO_2 thin films prepared by RF magnetron sputtering. *Appl. Surf. Sci.* **257**, 10869–10875 (2011).
95. Mirsafaei, M. et al. Sputter-deposited titanium oxide layers as efficient electron selective contacts in organic photovoltaic devices. *ACS Appl. Energy Mater.* **3**, 253–259 (2019).
96. Tauc, J. (Amsterdam: North-Holland Publishing Company, 1972).
97. Al-Kuhaili, M. Electromodulated transmittance of optical transitions in tungsten oxide. *J. Phys. Chem. Solids* **139**, 109317 (2020).
98. Arifuzzaman, M., Saha, T., Podder, J., Al-Bin, F. & Das, H. N. Effect of silver doping on the band gap tuning of tungsten oxide thin films for optoelectronic applications. *Heliyon* **10**, 6 (2024).
99. He, X. et al. Synthesis and optical properties of tantalum oxide films prepared by ionized plasma-assisted pulsed laser deposition. *Solid State Commun.* **147**, 90–93 (2008).
100. Lee, Y.-H. et al. Photo-induced atomic layer deposition of tantalum oxide thin films from Ta $(OC_2H_5)_5$ and O_2. *J. Electrochem. Soc.* **151**, C52 (2003).
101. Wei, A., Ge, Z., Zhao, X., Liu, J. & Zhao, Y. Electrical and optical properties of tantalum oxide thin films prepared by reactive magnetron sputtering. *J. Alloys Compd.* **509**, 9758–9763 (2011).

102. Shvets, V. et al. Electronic structure and charge transport properties of amorphous Ta_2O_5 films. *J. Non-cryst. Solids* **354**, 3025–3033 (2008).
103. Mazur, M. et al. Analysis of amorphous tungsten oxide thin films deposited by magnetron sputtering for application in transparent electronics. *Appl. Surf. Sci.* **570**, 151151 (2021).
104. Chen, H. et al. Tungsten oxide films by radio-frequency magnetron sputtering for near-infrared photonics. *Opt. Mater.: X* **12**, 100093 (2021).
105. Mohamed, S., Anders, A., Montero, I. & Galan, L. Structural and optical evaluation of WO_xNy films deposited by reactive magnetron sputtering. *J. Phys. Chem. of Solids* **68**, 2227–2232 (2007).
106. Mohamed, S., Mohamed, H. & Abd El Ghani, H. Development of structural and optical properties of WO_x films upon increasing oxygen partial pressure during reactive sputtering. *Phys. B: Condens. Matter* **406**, 831–835 (2011).
107. Tong, M., Dai, G., Wu, Y., He, X. & Gao, D. WO_3 thin film prepared by PECVD technique and its gas sensing properties to NO_2. *J. Mater. Sci.* **36**, 2535–2538 (2001).
108. Hadia, N., Alqahtani, M. S. & Mohamed, S. WO_3 nanowires for optoelectronic and gas sensing applications. *Appl. Phys. A* **119**, 1261–1267 (2015).
109. Mohamed, S. H. & Anders, A. Structural, optical, and electrical properties of WO_x (Ny) films deposited by reactive dual magnetron sputtering. *Surf. Coat. Technol.* **201**, 2977–2983 (2006).
110. Kalanur, S. S., Hwang, Y. J., Chae, S. Y. & Joo, O. S. Facile growth of aligned WO_3 nanorods on FTO substrate for enhanced photoanodic water oxidation activity. *J. Mater. Chem. A* **1**, 3479–3488 (2013).
111. Enesca, A., Duta, A. & Schoonman, J. Influence of tantalum dopant ions (Ta5+) on the efficiency of the tungsten trioxide photoelectrode. *Phys. Status Solidi (a)* **205**, 2038–2041 (2008).
112. Abd El-Rahman, A. & Mohamed, S. Preparation and characterization of nanostructured titanium oxynitride films for the application in self-cleaning and photoelectrochemical water splitting. *Thin Solid Films* **698**, 137864 (2020).
113. El-Rahman, A. A., Rabia, M. & Mohamed, S. Nitrogen doped TiO_2 films for hydrogen generation and optoelectronic applications. *J. Mater. Sci.: Mater. Electron.* **34**, 1149 (2023).
114. Pai, H. et al. Enhanced photocurrent density for photoelectrochemical catalyzing water oxidation using novel W-doped BiVO4 and metal organic framework composites. *J. Colloid Interface Sci.* **624**, 515–526 (2022).
115. Torad, E., Ismail, E. H., Mohamed, M. M. & Khalil, M. M. Tuning the redox potential of Ag@ Ag_2O/WO_3 and Ag@ Ag_2S/WO_3 photocatalysts toward diclofenac oxidation and nitrophenol reduction. *Mater. Res. Bull.* **137**, 111193 (2021).

Acknowledgements

Author contributions
H.Naghshara and S. Jafarpour are wrote the manuscript. H.Naghshara and S. Jafarpour prepared all of images. All authors reviewed the manuscript.

Declarations

Competing interests
The authors declare no competing interests.

Additional information
Supplementary Information The online version contains supplementary material available at https://doi.org/10.1038/s41598-025-92008-6.

Correspondence and requests for materials should be addressed to H.N.

Reprints and permissions information is available at www.nature.com/reprints.

Publisher's note Springer Nature remains neutral with regard to jurisdictional claims in published maps and institutional affiliations.